

Research Article

Radiation Analysis for Two Trajectory Points of the Fire II Entry

Romain Savajano,¹ Daniel F. Potter,² Ojas Joshi,¹ and Pénélope Leyland¹

¹ Ecole Polytechnique Fédérale de Lausanne, Interdisciplinary Aerodynamics Group, Station 9, 1015 Lausanne, Switzerland

² Centre for Hypersonics, University of Queensland, St Lucia, QLD 4072, Australia

Correspondence should be addressed to Romain Savajano, romain.savajano@epfl.ch

Received 26 July 2011; Revised 21 October 2011; Accepted 25 October 2011

Academic Editor: I. D. Boyd

Copyright © 2012 Romain Savajano et al. This is an open access article distributed under the Creative Commons Attribution License, which permits unrestricted use, distribution, and reproduction in any medium, provided the original work is properly cited.

Numerical rebuilding of two trajectory points ($t = 1634$ s and $t = 1643$ s) of the Fire II mission has been carried out to predict the radiative heat flux for nonequilibrium and close-to-equilibrium conditions. The simulations have been performed with *eilmer3* in an uncoupled way and using a tangent slab method for the radiation transport. Different population models (QSS and Boltzmann) have been compared, and the influence of catalytic wall condition was taken into account. An analysis on the spectral range and on the spectral resolution has also been carried out.

1. Introduction

During atmospheric (re)entries, planetary probes encounter high heat fluxes due to their significant speed (up to 11 km/s for an Earth reentry). Such excessive thermal loads can damage the on-board equipment and compromise the safety of the passengers in case of a manned-flight mission. As a consequence, the sizing of the thermal protection system (TPS) is a crucial step in the preliminary design study of a probe.

The Fire II mission took place in May 22nd, 1965 [1]. Its main goal was the assessment of the radiative heating environment during an Earth reentry. The vehicle geometry was an Apollo type with a reentry velocity of 11.4 km/s. The fore body consisted in a three layer configuration formed by phenolic-asbestos heat-shield sandwiched between beryllium calorimeters. The contribution from the radiation of the hot plasma to the total heat flux received by the probe was up to 40%. This paper concentrates on this radiative contribution. The reconstruction of radiation spectra for the Fire II experiment has been already discussed in numerous papers [2–4].

Two points of the trajectory of the Fire II mission have been numerically rebuilt. The first one at $t = 1634$ s corresponds to nonequilibrium conditions whereas the second one at $t = 1643$ s is close to equilibrium conditions, even if a small region behind the shock is nonequilibrium. Figure 1 gives the temperature profiles of the translational-rotational

temperature and the vibrational-electronic temperature for the two simulations.

In this work, the code retained for the simulations is *eilmer3*, a multiblock compressible Navier-Stokes solver described in Section 2. Section 3 is dedicated to the results of the simulations.

An analysis of the spectral range has been performed to assess the wavelength range of interest and the number of points needed for a good accuracy. Then two different population models (QSS and Boltzmann) have been compared and the influence of the catalytic wall condition discussed. Finally, a comparison with the flight data taken by the calorimeters was made.

2. Description of Flow Field Solver

In this work, the *eilmer3* [5, 6] multiblock compressible Navier-Stokes solver was used to generate the CFD solutions. The implementation of the governing equations, diffusion model, and radiation transport models in *eilmer3* are presented in Section 2.1. *Eilmer3* makes use of external gas property and thermochemical nonequilibrium modules, which are described in Section 2.2 and 2.3.

2.1. Axisymmetric Navier-Stokes Solver: Eilmer3. The *eilmer3* code is a multiple block-structured finite volume code. It is

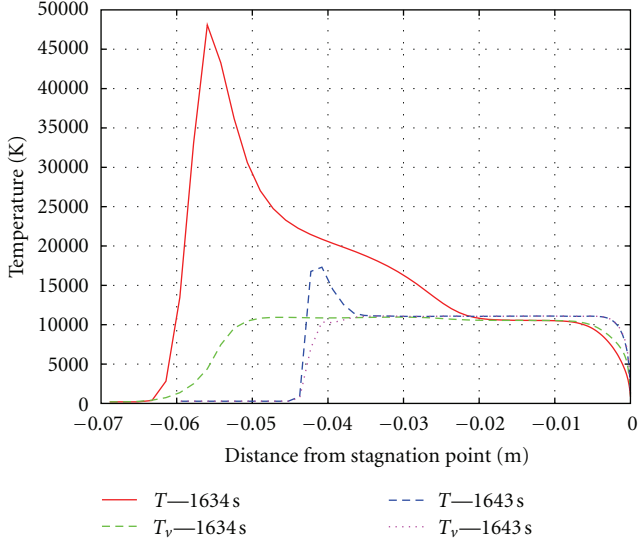


FIGURE 1: Temperature profiles on the stagnation line for the two trajectory points.

capable of considering planar, axisymmetric, and fully three-dimensional geometries; only the axisymmetric formulations are considered here.

2.1.1. Implementation of the Governing Equations. The code solves the compressible Navier-Stokes equations via a cell-centred time-dependent finite-volume formulation:

$$\frac{\partial}{\partial t} \int_V U dV = - \int_S (\bar{F}_i - \bar{F}_v) \cdot \hat{n} dA + \int_V Q dV. \quad (1)$$

In the present work, a two-temperature formulation of the Navier-Stokes equations is implemented. The inviscid gas-dynamics, viscous effects, finite-rate chemistry, and thermal energy exchange are treated with an operator-split approach, where the respective flux vectors and source terms are applied in a loosely coupled manner. The vector of conserved quantities therefore consists of total mass, total momentum, total energy, vibration-electron-electronic energy, and species mass:

$$U = \begin{bmatrix} \rho \\ \rho u_x \\ \rho u_y \\ \rho E \\ \rho e_{ve} \\ \rho f_s \end{bmatrix}, \quad (2)$$

where ρ is density, u is velocity, E is total energy, e_{ve} is the vibration-electron-electronic energy, and f_s is the species s mass-fraction. Both total and species masses are considered in order to implement the mass-conserved formulation of the chemical kinetic ODE system proposed by Gollan [7]. In contrast, translation-rotation energy is not considered as a

conserved quantity as it can be calculated from the definition of total energy. The inviscid flux vector components are

$$\bar{F}_i = \begin{bmatrix} \rho u_x \\ \rho u_x^2 + p \\ \rho u_y u_x \\ \rho E u_x + p u_x \\ \rho e_{ve} u_x + p_e u_x \\ \rho f_s u_x \end{bmatrix} \hat{i} + \begin{bmatrix} \rho u_y \\ \rho u_x u_y \\ \rho u_y^2 + p \\ \rho E u_y + p u_y \\ \rho e_{ve} u_y + p_e u_y \\ \rho f_s u_y \end{bmatrix} \hat{j}, \quad (3)$$

where p_e is the electron pressure, and the viscous component is

$$F_v = \begin{bmatrix} 0 \\ \tau_{xx} \\ \tau_{yx} \\ \tau_{xx} u_x + \tau_{yx} u_y + q_x \\ q_{x,ve} \\ J_{x,s} \end{bmatrix} \hat{i} + \begin{bmatrix} 0 \\ \tau_{xy} \\ \tau_{yy} \\ \tau_{xy} u_x + \tau_{yy} u_y + q_y \\ q_{y,ve} \\ J_{y,s} \end{bmatrix} \hat{j}, \quad (4)$$

where τ denotes the axisymmetric viscous stress components, q is heat flux, and J is diffusion flux. The vector of source terms is separated into geometric, chemical kinetic, thermal energy exchange, and radiation contributions in order to apply the operator-splitting integration approach:

$$Q = Q_{\text{geom.}} + Q_{\text{chem.}} + Q_{\text{therm.}} + Q_{\text{rad.}}, \quad (5)$$

where

$$Q_{\text{geom.}} = \begin{bmatrix} 0 \\ 0 \\ (p - \tau_{\theta\theta}) A_{xy} / V \\ 0 \\ 0 \\ 0 \end{bmatrix},$$

$$Q_{\text{chem.}} = \begin{bmatrix} 0 \\ 0 \\ 0 \\ 0 \\ \sum_m^{N_{\text{mol.}}} \Omega_m^{VC} + \sum_i^{N_{\text{ion.}}} \Omega_i^{EC} \\ M_s \dot{\omega}_s \end{bmatrix},$$

$$\begin{aligned}
Q_{\text{therm.}} &= \begin{bmatrix} 0 \\ 0 \\ 0 \\ 0 \\ \sum_m^{N_{\text{mol.}}} \Omega_m^{VT} + \sum_s^{N_{\text{species}}} \Omega_s^{ET} \\ 0 \end{bmatrix}, \\
Q_{\text{rad.}} &= \begin{bmatrix} 0 \\ 0 \\ 0 \\ -\nabla \cdot \vec{q}_{\text{rad}} \\ -\nabla \cdot \vec{q}_{\text{rad}} \\ 0 \end{bmatrix}.
\end{aligned} \tag{6}$$

Here A_{xy} is the cell area, M_s is the species mole weight, $-\nabla \cdot \vec{q}_{\text{rad}}$ is the radiative source term (included in both total and vibration-electronic-electron energies), and Ω^{VC} , Ω^{EC} , Ω^{VT} , and Ω^{ET} are the source terms for vibration-chemistry coupling, electron-chemistry coupling, vibration-translation exchange, and electron-translation exchange, respectively.

2.1.2. Integration, Flux Calculators, and Boundary Conditions.

The inviscid and viscous flux vectors are integrated via a predictor-corrector method, the chemical source terms via an α -QSS method, and the energy source terms via a fourth order Runge-Kutta method. The radiative source terms are fully coupled with the inviscid update but are not reevaluated for the corrector step. The inviscid fluxes are computed via a dissipative equilibrium flux method [8] in the vicinity of shocks and the AUSMDV [9] scheme elsewhere. Boundary conditions are applied via two layers of ghost cells surrounding the computational domain.

2.1.3. Diffusion. The effective diffusion coefficients \tilde{D}_i for all neutral species are calculated in a simple manner by assuming a constant Lewis number:

$$\tilde{D}_i = \frac{\mathcal{L}_e \mu}{\mathcal{P}_r}, \tag{7}$$

where \mathcal{P}_r is the Prandtl number and $\mathcal{L}_e = 1.4$ for reacting air. For ions, the ambipolar correction proposed by Gnoffo et al. [10] is implemented to maintain charge neutrality. The diffusive mass flux of species i is then calculated according to the approximate form of Fick's first law:

$$\vec{J}_i = -\rho \tilde{D}_i \nabla f_i. \tag{8}$$

2.2. High-Temperature Gas Property Module

2.2.1. Thermodynamic Coefficients. The thermodynamic coefficients for partially ionised gases in the Ar-C-N-O elemental system are calculated based on the assumption of fully decoupled internal thermal modes. For the air test-gas in the present work, the 11 species considered are N_2 , N_2^+ , NO , NO^+ , O^2 , O_2^+ , N , N^+ , O , O^+ , and e^- . Negative

TABLE 1: Summary of the collisional-radiative mechanisms implemented for N and O in N_2 - O_2 mixtures.

Species	CR mechanisms	Models
N	Electron impact excitation	(a) Frost et al. [21] (b) Gryziński [22]
	Electron impact ionization	(a) Soon and Kunc [23] (b) Panesi [24]
	Radiative decay	NIST ASD [16]
O	Electron impact excitation	(a) Zatsarinny and Tayal [25] (b) Gryziński [22]
	Electron impact ionization	(a) Soon and Kunc [23] (b) Panesi [24]
	Radiative decay	NIST ASD [16]

TABLE 2: Forward (T_f) and backward (T_b) rate-controlling temperatures for bulk chemical kinetics.

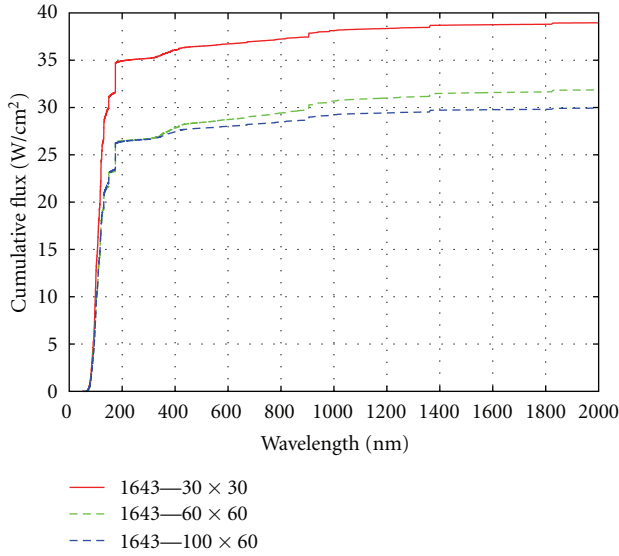
Reaction type	T_f	T_b
Heavy-particle impact dissociation	$T_{\text{vib}}^s, T_{\text{trans}}^{s-1}$	T_{trans}
Electron impact dissociation	$T_{\text{vib}}^s, T_e^{s-1}$	T_e
Exchange	T_{trans}	T_{trans}
Associative ionisation	T_{trans}	T_{trans}
Electron-impact ionisation	T_e	T_e

TABLE 3: Flow conditions for the Fire II reentry trajectory.

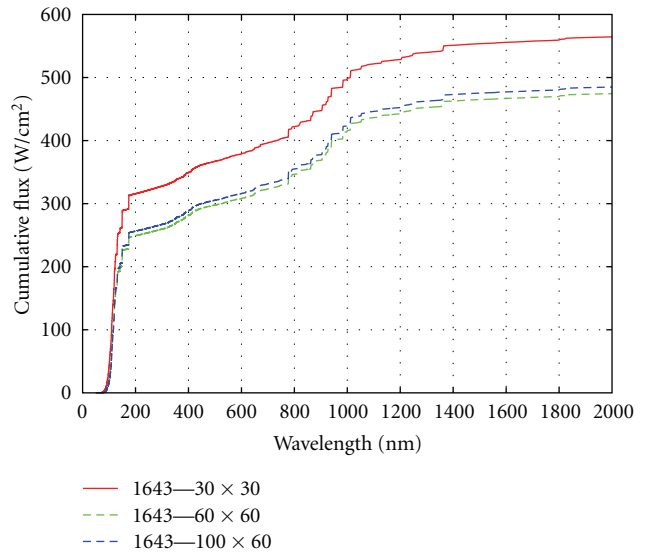
Time from launch (s)	Heat-shield 1	Heat-shield 2
	1634	1643
Altitude (km)	76.42	53.04
Velocity, u_∞ (km/s)	11.36	10.48
Density, ρ_∞ (10^{-4} kg/m ³)	0.37	7.80
Pressure, p_∞ (Pa)	2.09	62.04
Temperature, T_∞ (K)	195	276
Wall temperature, T_w (K)	615	640

ions are not considered based on their low concentrations. Translation and rotation are modelled under the assumption of full excitation. Molecular vibration is described by the truncated harmonic oscillator model. The thermodynamic contributions of the electronic thermal modes are calculated by direct summation over the electronic levels, truncated at specific levels that maximise the efficiency and accuracy of the calculation. Comparisons with the CEA2 code [11] demonstrate good agreement for molecules up to temperatures of 5,000 K and good agreement for atoms up to temperatures of 11,000 K. The errors found above these temperature ranges are due to the assumption of fully decoupled thermal modes and are unavoidable for the generalised multitemperature context the module was designed for.

2.2.2. Transport Coefficients. The thermal nonequilibrium transport coefficients are calculated via the multicomponent mixture rules proposed by Gupta et al. [12]. The collision integrals recommended by Wright and Levin [13] and Wright et al. [14, 15] are preferred over those given in [12]



(a) 1634s



(b) 1643s

FIGURE 2: Grid convergence analysis.

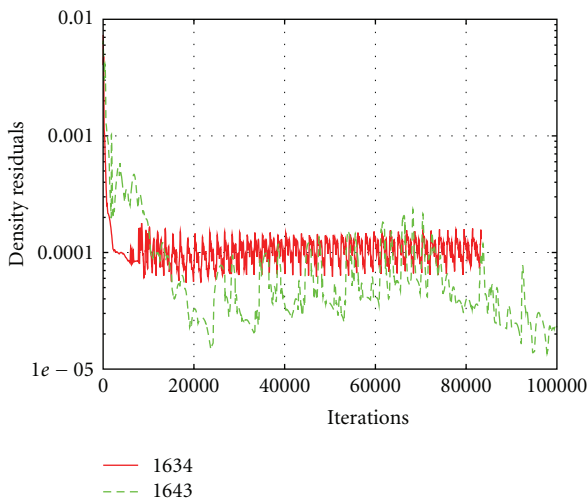


FIGURE 3: Density residuals.

as the former are based on recent computational chemistry calculations where available. Good agreement is found with the CEA2 code [11] for the viscosity of equilibrium air in the temperature range $1,000 \leq T \leq 20,000$ K.

2.2.3. Spectral Radiation Coefficients. The spectral radiation coefficients are calculated by an in-house line-by-line model for atomic and diatomic bound-bound transitions, and curve-fits and hydrogenic approximations for continuum transitions. Electronic level and atomic line data were obtained from NIST [16], and the diatomic electronic transition moments presented by Chauveau et al. [17] and Babou et al. [18] are implemented. Following the recommendations of Johnston [19], atomic lines are modelled individually for

$\Delta E_{ul} \geq 6$ eV and as multiplets for $\Delta E_{ul} < 6$ eV. For diatomic radiators, $^2\Sigma-^2\Sigma$ transitions are modelled via Hund's case (b), $^2\Sigma-^2\Pi$ transitions are modelled via the intermediate (a)-(b) case, and the remaining transitions are modelled via Hund's case (a). Continuum transitions were modelled by the step model of Johnston [19] for N and O photoionisation and with hydrogenic approximations otherwise. The model implementation has been verified by comparisons with the SPRADIAN07 code [20].

Electronic level populations for N_2 , N_2^+ , N, and O are calculated by a collisional-radiative model applied in the QSS limit. The other radiators considered in this work (N^+ and O^+) are assumed to be populated by Boltzmann distributions. For N_2 and N_2^+ , the rate coefficient models compiled by Johnston [19] are implemented. For N and O, the mechanisms considered are (1) electron impact excitation, (2) electron impact ionisation, and (3) bound-bound radiative transitions. The models implemented for each, in order of preference, are summarised in Table 1. Experiment or computational chemistry based rate coefficients are preferred for low lying levels, while simple hydrogenic models are implemented for the remainder.

2.3. Thermochemical Nonequilibrium Module

2.3.1. Chemical Kinetics. The chemical kinetics of bulk species are considered by both flow solvers (as opposed to electronically or vibrationally specific models). The rate-controlling temperature approach for modelling reactions in thermal nonequilibrium is adopted; the rate-controlling temperatures for the various classes of reactions considered are summarised in Table 2. Following the recommendations of Lino da Silva et al. [26], the vibrational temperature exponent s is set to 0.7 for compression flows and 0.5 for expansion flows. The forward rates k_f from the 11 species

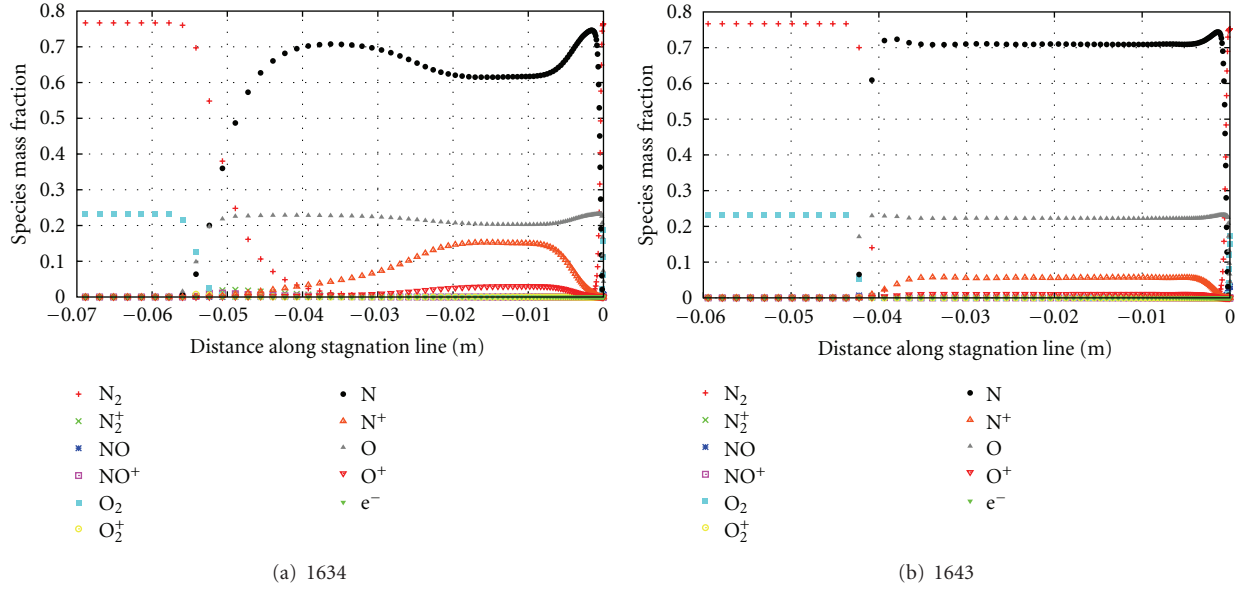


FIGURE 4: Species mass fractions on the stagnation line.

air reaction scheme proposed by Park [27] are implemented; however, the radiative recombination reactions are omitted. The backward rates k_b for these reactions are calculated as

$$k_b(T_b) = \frac{k_f(T_b)}{K_c(T_b)}, \quad (9)$$

where the equilibrium constant K_c is calculated via the Gibbs free energy approach.

2.3.2. Thermal Energy Exchange. Vibration-translation exchange is modelled via the Landau-Teller equation. The relaxation times are calculated by the Millikan and White [28] expressions with the high-temperature correction proposed by Park [27]. The heating of electrons through elastic collisions with heavy particles is modelled by the rate equation derived by Appleton and Bray [29]. For Coulomb collisions between electrons and ions, the effective collision frequency is derived from [29], and the effective collision frequency for electron-neutral interactions is calculated via the curve fits given by Gnoffo et al. [10].

3. Fire II Simulations

3.1. Flow Conditions. In this work two trajectory points of the Fire II flight experiment are considered: $t = 1634$ s and $t = 1643$ s. Consequently, a nonequilibrium case and a close-to-equilibrium case can be considered. Table 3 gives the flow conditions for these two trajectory points [1].

For all the simulations, a two-temperature model was assumed: $T_{tr,rot}$ and $T_{vib,el}$. Simulations have been performed with both noncatalytic and super catalytic wall conditions (recombination to the inflow conditions). The influence of this boundary condition on the radiative heat flux is discussed in Section 3.3.4.

3.2. Grid Convergence. The simulation strategy is the same for the two trajectory points. Start the simulations on a coarse grid without any viscous effects and chemical reactions. After one body length, the chemical reactions are started, then after another body length the viscous effects are progressively taken into account. Several body lengths are then necessary to ensure the good convergence of the simulations. Three different meshes were used in order to reach a converged solution: 30×30 , 60×60 , and 100×60 . Figure 2 shows the convergence of the radiative heat flux at the stagnation point, and Figure 3 gives the density residuals evolution for the two trajectory points. The final mesh retained for analysis in both cases was a 100×60 grid refined at the wall.

3.3. Radiation Analysis. For the two trajectory points, the radiative heat flux at the stagnation point has been evaluated through uncoupled simulations with a tangent slab method [30] (100 cells per row are considered) for the radiation transport.

The divergence for a cell i is given by

$$(\nabla \cdot q_{rad})_i = \left(\frac{\partial q_{rad}}{\partial s} \right)_i \approx \frac{q_{rad}^{i+1} - q_{rad}^i}{\Delta s_i}. \quad (10)$$

As discussed in Section 2, the only species considered for radiation are N_2 , N_2^+ , N , N^+ , O , and O^+ . NO was not included as a radiating species as its concentration was almost null. Figure 4 shows the species mass fractions on the stagnation line for the two trajectory points. It can be noticed that 95% of the flow after the shock is composed of N , O , and N^+ .

3.3.1. Spectral Range Analysis. First, simulations were performed to assess the wavelength range necessary for the

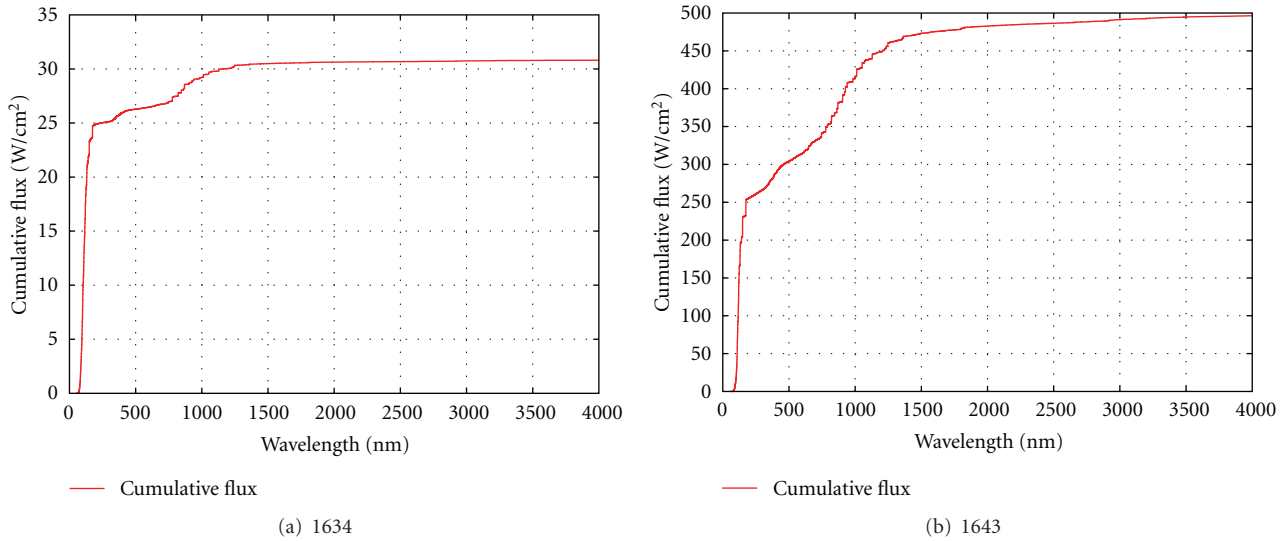


FIGURE 5: Spectral range analysis.

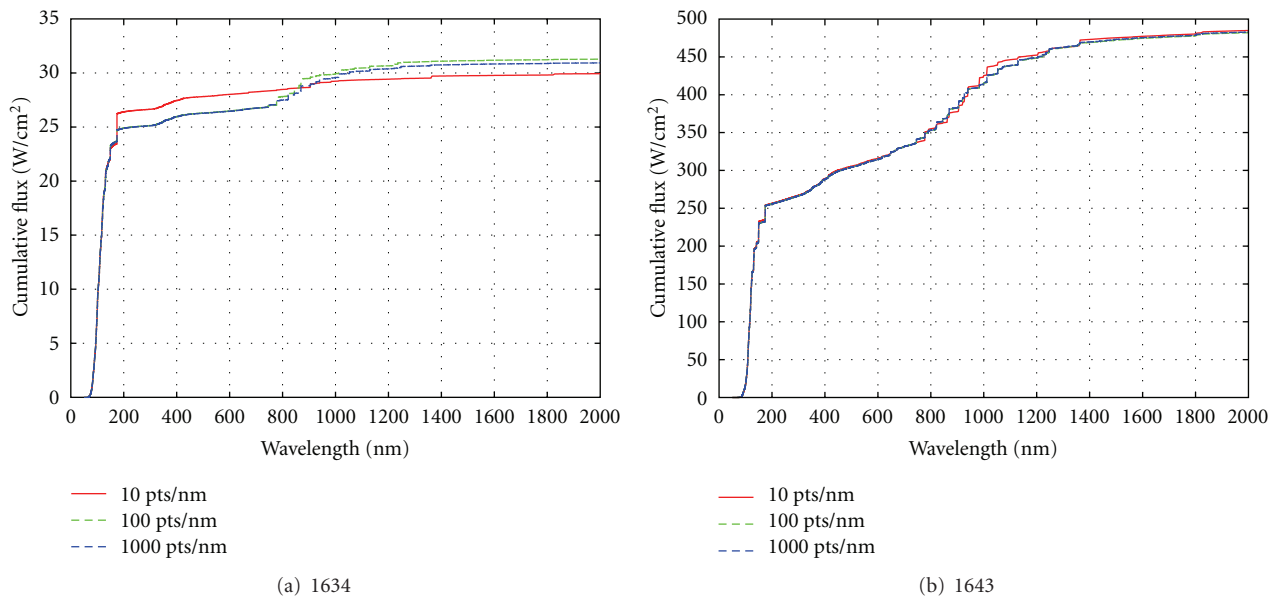


FIGURE 6: Spectral resolution analysis.

study. The range 50 to 4000 nm was considered with a spectral resolution of 100 points per nm. The results obtained are displayed in Figure 5.

In both cases, it can be noticed that 98% of the contribution is coming from wavelengths between 50 and 2000 nm. For further analysis, the spectral range of study can then be reduced to 50 to 2000 nm.

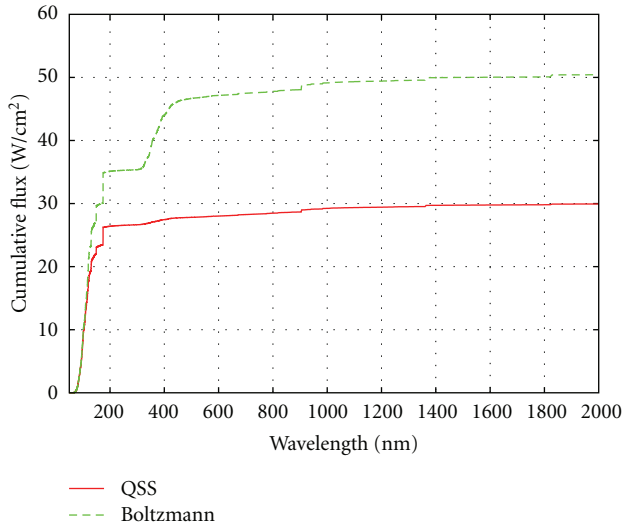
3.3.2. Spectral Resolution Analysis. For the two trajectory points, a study has been performed on the influence of the spectral resolution. Simulations with 10, 100, and 1000 points per nm have been done. The results are plotted in Figure 6.

In both cases, the conclusion can be made that 100 points per nm are sufficient for computing the radiative heat flux.

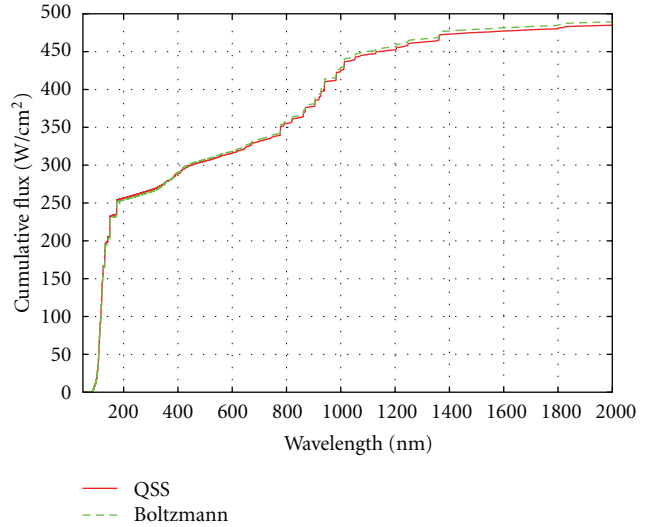
3.3.3. Boltzmann versus QSS. After the discussions on spectral ranges and resolutions, two population models have been compared: Boltzmann and QSS approximation. Figure 7 give the results obtained.

As expected, for the low density case ($t = 1634$), which is completely at nonequilibrium, simulations with Boltzmann model are clearly overestimating the radiative heat flux, whereas at the higher density case, close to thermal equilibrium, the two models are giving almost the same results.

3.3.4. Super Catalytic Wall versus Noncatalytic Wall. The Fire II on-board equipment was protected by heat shields

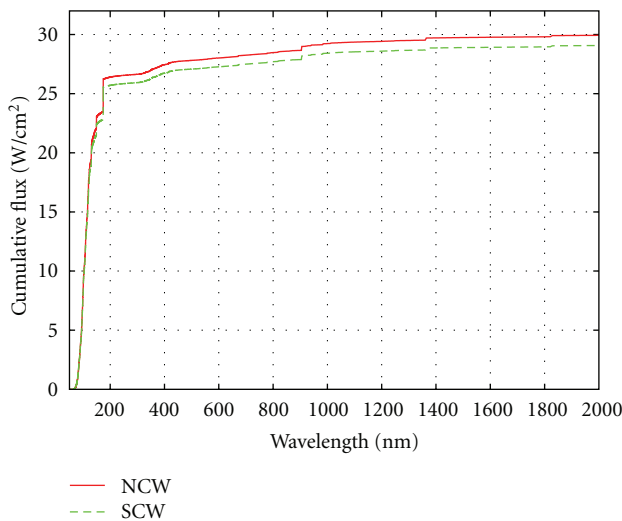


(a) 1634

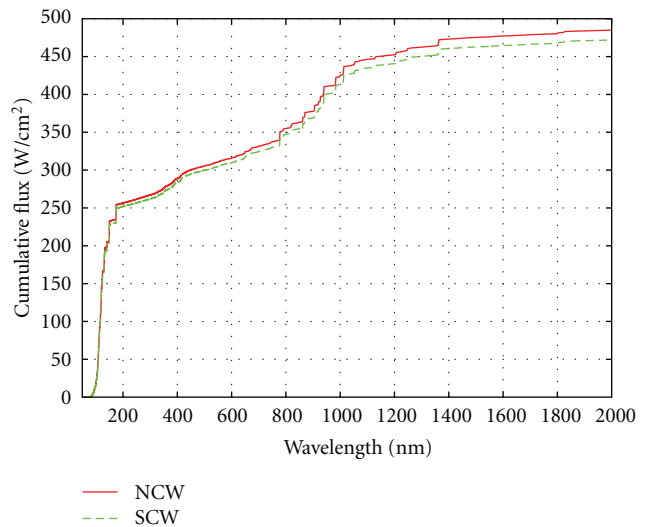


(b) 1643

FIGURE 7: QSS versus Boltzmann.



(a) 1634



(b) 1643

FIGURE 8: Influence of the super catalytic wall condition.

containing beryllium which is highly catalytic to reactions. Consequently, the first assumptions were to consider the wall as fully catalytic [4]. However as explained by Olynick et al. [3], due to the presence of oxygen in the flow, the beryllium is likely to be oxidised and thus having less catalytic effects. For the two trajectory points, simulations were performed with and without the catalytic wall condition. Figure 8 shows the radiative intensity obtained in both cases.

For the two trajectory points, the catalytic wall condition leads to a lower heat flux but the two values are still pretty close.

3.3.5. *Comparison with Flight Data.* The results obtained for the stagnation point can be compared with flight data [1] using the data measured by the calorimeter and the radio-

meter. The calorimeter has measured the total heating rate minus the radiative flux absorbed by the beryllium shield, that is, $q_{conv} + \alpha q_{rad}$, where α is the absorptance of the beryllium heat shield. The radiometer value gives directly the value for the radiative heat flux. However, the VUV contribution is not taken into account in this measure. In Figure 9, a comparison is given with values obtained from the simulations in this work. It can be noticed that there is a discrepancy between the values from the calorimeter and the values obtained here when using the authors convective heat flux value. However, when using an average value for the convective heat flux (independently of the catalytic wall condition) coming from previous works [2–4, 31], the agreement is much more better. It is explained by the fact that the diffusive heat flux is not taken into account correctly in

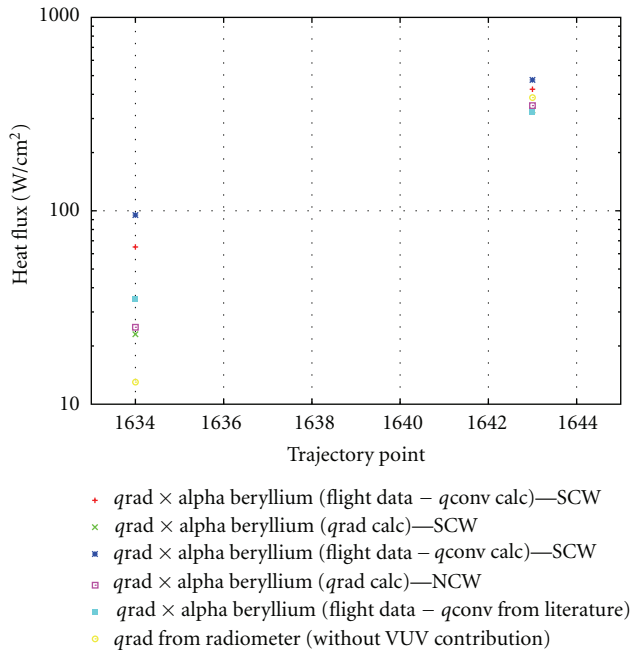


FIGURE 9: Comparison with flight data for the stagnation point.

the evaluation of the convective heat flux in our simulations. For the comparison with the radiometer, the trajectory point at 1634s is in good agreement (regarding the fact that a major contribution from VUV has been calculated). However, for the 1643s trajectory point, the radiative heat flux calculated seems to be too low in comparison with the flight data.

4. Conclusions

In this work, the uncoupled radiative heat flux for two trajectory points of the Fire II experiment has been rebuilt with a tangent slab model. It was first shown that the entire radiative heat flux was coming from the wavelength range 50 to 2000 nm and that 100 points per nm were sufficient to get a good accuracy with a tangent slab approach. It has also been confirmed that for $t = 1643$ s, the flow is close to the thermal equilibrium as the two different population models (Boltzmann and QSS) are leading to the same results, whereas at $t = 1634$ s, there is a strong discrepancy between the two methods. As for the catalytic wall condition, its influence on the radiative heat flux is negligible for the two trajectory points. The results obtained for the radiative heat flux are in good agreement with flight data.

Acknowledgment

This work was partially supported by the ESA-NPI Program, CCN C21872.

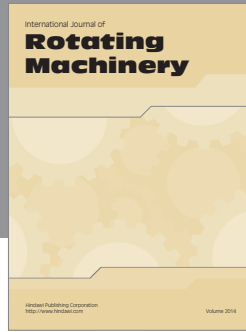
References

- [1] D. L. Cauchon, "Radiative heating results from the FIRE II flight experiment at a re-entry velocity of 11. km/s," Tech. Rep. TM X-1402, NASA, 1967.

- [2] C. O. Johnston and B. R. Hollis, "Nonequilibrium stagnation-line radiative heating for Fire II," *Journal of Spacecraft and Rockets*, vol. 45, no. 6, pp. 1185–1195, 2008.
- [3] D. R. Olynick, W. D. Henline, L. H. Chambers, and G. V. Candler, "Comparison of coupled radiative flow solutions with project fire II flight data," *Journal of Thermophysics and Heat Transfer*, vol. 9, no. 4, pp. 586–594, 1995.
- [4] R. B. Greendyke and L. C. Hartung, "Convective and radiative heat transfer analysis for the fire II forebody," *Journal of Spacecraft and Rockets*, vol. 31, no. 6, pp. 986–992, 1994.
- [5] P. A. Jacobs, "MB CNS: a computer program for the simulation of transient compressible flows; 1998 update," Tech. Rep. 7/98, Department of Mechanical Engineering, The University of Queensland, Brisbane, Australia, 1998.
- [6] D. Potter, S. Karl, and P. Leyland, "TN032—EPFL Contribution to ESA-TRP AMOD," Tech. Rep., ESA, 2009.
- [7] R. J. Gollan, *Computational modelling of high-temperature gas effects with application to hyper-sonic flows*, Ph.D. thesis, School of Engineering, The University of Queensland, June 2008.
- [8] M. N. Macrossan, "The equilibrium flux method for the calculation of flows with non-equilibrium chemical reactions," *Journal of Computational Physics*, vol. 80, no. 1, pp. 204–231, 1989.
- [9] Y. Wada and M. S. Liou, "A flux splitting scheme with high-resolution and robustness for discontinuities," Tech. Rep. 94-0083, AIAA, January 1994.
- [10] P. A. Gnoffo, R. N. Gupta, J. L. Shinn, and United States, "Conservation equations and physical models for hypersonic air flows in thermal and chemical equilibrium," Tech. Rep. TP-2867, NASA, 1989, Book, microform.
- [11] B. J. McBride and S. Gordon, "Computer program for calculation of complex chemical equilibrium compositions and applications, part 2: users manual and program description," Tech. Rep. 1311, NASA, 1996.
- [12] R. N. Gupta, J. M. Yos, R. A. Thompson, and K. Lee, "A review of reaction rates and thermodynamic and transport properties for an 11-species air model for chemical and thermal nonequilibrium calculations to 30000 K," Tech. Rep., NASA STI/Recon, August 1990.
- [13] M. J. Wright and E. Levin, "Collision integrals for ion-neutral interactions of air and argon," *Journal of Thermophysics and Heat Transfer*, vol. 19, no. 1, pp. 127–128, 2005.
- [14] M. J. Wright, D. Bose, G. E. Palmer, and E. Levin, "Recommended collision integrals for transport property computations, part 1: air species," *AIAA Journal*, vol. 43, no. 12, pp. 2558–2564, 2005.
- [15] M. J. Wright, H. H. Hwang, and D. W. Schwenke, "Recommended collision integrals for transport property computations part 2: mars and venus entries," *AIAA Journal*, vol. 45, no. 1, pp. 281–288, 2007.
- [16] NIST Chemical Kinetics Database, Ver. 7.0, 2003.
- [17] S. Chauveau, M. Y. Perrin, P. Rivière, and A. Soufiani, "Contributions of diatomic molecular electronic systems to heated air radiation," *Journal of Quantitative Spectroscopy and Radiative Transfer*, vol. 72, no. 4, pp. 503–530, 2002.
- [18] Y. Babou, P. Riviere, M. Y. Perrin, and A. Soufiani, "High-temperature and non equilibrium partition function and thermodynamic data of diatomic molecules," *International Journal of Thermophysics*, vol. 30, pp. 416–438, 2009.
- [19] C. Johnston, *Nonequilibrium shock-layer radiative heating for Earth and Titan entry*, Ph.D. thesis, Virginia Polytechnic Institute and State University, Blacksburg, Va, USA, 2006.
- [20] S.-Y. Hyun, *Radiation code SPRADIAN07 and its applications*, Ph.D. thesis, School of Mechanical, Aerospace and Systems

Engineering, Division of Aerospace Engineering, KAIST, Daejeon, Korea, 2009.

- [21] R. M. Frost, P. Awakowicz, H. P. Summers, and N. R. Badnell, "Calculated cross sections and measured rate coefficients for electron-impact excitation of neutral and singly ionized nitrogen," *Journal of Applied Physics*, vol. 84, no. 6, pp. 2989–3003, 1998.
- [22] M. Gryziński, "Classical theory of electronic and ionic inelastic collisions," *Physical Review*, vol. 115, no. 2, pp. 374–383, 1959.
- [23] W. H. Soon and J. A. Kunc, "Thermal nonequilibrium in partially ionized atomic oxygen," *Physical Review A*, vol. 41, no. 2, pp. 825–843, 1990.
- [24] M. Panesi, *Physical models for nonequilibrium plasma flow simulations at high speed re-entry conditions*, Ph.D. thesis, von Karman Institute for Fluid Dynamics, Rhode-Saint-Genèse, Belgium, 2009.
- [25] O. Zatsarinny and S. S. Tayal, "Electron collisional excitation rates for O I using the B-spline R-matrix approach," *Astrophysical Journal, Supplement Series*, vol. 148, no. 2, pp. 575–582, 2003.
- [26] M. Lino da Silva, V. Guerra, and J. Loureiro, "Two-temperature models for nitrogen dissociation," *Chemical Physics*, vol. 342, no. 1–3, pp. 275–287, 2007.
- [27] C. Park, "Review of chemical-kinetic problems of future NASA missions, I: earth entries," *Journal of Thermophysics and Heat Transfer*, vol. 7, no. 3, pp. 385–398, 1993.
- [28] R. C. Millikan and D. R. White, "Systematics of vibrational relaxation," *The Journal of Chemical Physics*, vol. 39, no. 12, pp. 3209–3213, 1963.
- [29] J. P. Appleton and K. N. C. Bray, "The conservation equations for a nonequilibrium plasma," *Journal of Fluid Mechanics*, vol. 20, no. 4, pp. 659–672, 1964.
- [30] M. F. Modest, *Radiative Heat Transfer*, Academic Press, London, UK, 2nd edition, 2003.
- [31] G. E. Palmer, T. White, and A. Pace, "Direct coupling of the NEQAIR radiation and DPLR computational fluid dynamic codes," *Journal of Spacecraft and Rockets*, vol. 48, pp. 836–845, 2011.



Hindawi

Submit your manuscripts at
<http://www.hindawi.com>

